Tandem MS imaging and *in situ* characterization of bioactive wood metabolites in Amazonian tree species *Sextonia rubra*

Tingting Fu,[†‡] David Touboul,[†] Serge Della-Negra,[‡] Emeline Houël,[§] Nadine Amusant,[‖] Christophe Duplais,[§] Gregory L. Fisher,[⊥*] and Alain Brunelle[†*]

† Institut de Chimie des Substances Naturelles, CNRS UPR 2301, Univ. Paris-Sud, Université Paris-Saclay, Avenue de la Terrasse, 91198 Gif-sur-Yvette, France

‡ Institut de Physique Nucléaire, UMR 8608, IN2P3-CNRS, Université Paris-Sud, Université Paris-Saclay, 91406 Orsay, France

§ CNRS, UMR EcoFoG, AgroParisTech, Cirad, INRA, Université des Antilles, Université de Guyane, 97300 Cayenne, France

‖ Cirad, UMR EcoFoG, AgroParisTech, CNRS, INRA, Université des Antilles, Université de Guyane, 97310 Kourou, France

⊥ Physical Electronics, Chanhassen, Minnesota, 55317 USA

ABSTRACT: Driven by a necessity for confident molecular identification at high spatial resolution, a new time-of-flight secondary ion mass spectrometry (TOF-SIMS) tandem mass spectrometry (tandem MS) imaging instrument has been recently developed. In this report, the superior MS/MS spectrometry and imaging capability of this new tool is shown for natural product study. For the first time, *via in situ* analysis of the bioactive metabolites rubrynolide and rubrenolide in Amazonian tree species *Sextonia rubra* (Lauraceae), we were able both to analyze and to image by tandem MS the molecular products of natural biosynthesis. Despite the low abundance of the metabolites in the wood sample(s), efficient MS/MS analysis of these γ-lactone compounds was achieved providing high confidence in the identification and localization. In addition, tandem MS imaging minimized the mass interferences and revealed specific localization of these metabolites primarily in the ray parenchyma cells but also in certain oil cells and, further, revealed the presence of previously unidentified γ-lactone paving the way for future studies in biosynthesis.

Biological TOF-SIMS has undergone rapid advances in the last two decades. This is principally due to the following developments: various cluster ion beams have brought multiple benefits including substantial ion yield enhancement by gold clusters,[1,2] bismuth clusters[3,4] and, in particular, buckminsterfullerene (C_{60}^{q+}),[5] while both C_{60}^{q+} and large argon clusters (*e.g.* $Ar_{2,500}^{+}$)[6] have extended the practical analytical mass range toward 10 kDa;[7,8] sub-micrometer imaging resolution in routine analyses is now relatively common;[9,10] finally, the capabilities for three dimensional imaging are now readily accessible.[11] Nevertheless, current mass spectrometry imaging analysis of biological samples is still dominated by matrix-assisted laser desorption ionization (MALDI).[12] Besides the inferior ability in generating high mass range spectra, a major limitation in TOF-SIMS is the lack of structural analysis for ion peak annotation.[13] Moreover, mass accuracy in TOF-SIMS is limited by the kinetic energy and emission angle distributions of the desorbed ions,[14] which makes unambiguous assignments extremely challenging. Consequently, tandem mass spectrometry is highly desired to help molecular identification, especially in the case of biological samples comprised of a complex chemical environment.

An early attempt of performing tandem mass spectrometry measurement with TOF-SIMS was achieved by Touboul, *et al.* using a post source decay (PSD)-like method.[15] Here no collision cell was integrated and the fragmentation spectrum depended on the metastable decomposition of the selected precursor ions. Based on a commercial hybrid quadrupole orthogonal TOF (Q-TOF) mass spectrometer, Carado, *et al.*[16,17] developed a hybrid MALDI/C_{60}-SIMS method which was able to provide CID fragmentation and relatively high mass resolution of 12,000-15,600 with a moderate lateral resolution of 25-30 µm. This hybrid system was later improved by Lanni, *et al.*[18] to image complex biological samples at 10 µm lateral resolution. Meanwhile, the Vickerman group designed the J105 3D Chemical Imager which exploited a linear buncher-TOF and a quasi-continuous C_{60} primary ion beam.[19,20] The new dedicated instrument offers MS/MS and high throughput cell imaging capabilities,[21] and has recently been applied to identify

intact lipids in *Drosophila* brain using an argon cluster ion source.[22] Smith, *et al.* reported the coupling of a C_{60} SIMS source to an FTICR mass spectrometer which allows MS/MS spectrometry with excellent mass resolution (> 100,000, $m/\Delta m$ 50%) and mass accuracy (< 2 ppm).[23] This instrumental coupling concept has also led to the launch of a new hybrid tandem mass spectrometer which couples a TOF-SIMS instrument with an Orbitrap mass analyzer, using an argon cluster ion source to probe the sample, thus enabling 2D- and 3D-imaging at < 5 µm lateral resolution with the high mass resolution and accuracy of the Orbitrap.[24]

Different from the above instrumental concepts pursuing conventional tandem MS analysis by sacrificing all the other ions or certain TOF-SIMS performance characteristics, the recent design of a new TOF-SIMS parallel imaging MS/MS spectrometer by Fisher and coauthors,[25,26] in contrast, enables parallel and lossless collection of MS and MS/MS spectra. This attribute ensures that any analytical volume of the sample would be used to the best. The parallel imaging MS/MS spectrometer is based on the triple ion focusing time-of-flight (TRIFT) analyzer, where a precursor selection device allows selection with a monoisotopic window. Furthermore, this system is fully comparable with conventional TOF-SIMS instruments in terms of sample handling, ion source operation and lateral resolution limit which proved to be problematic in other cases.[23,27]

As a further exploration of the analytical potential of this new technology, we herein report the application of the tandem MS imaging technique for *in situ* characterization of plant metabolites in Amazonian tree species *Sextonia rubra* (Mez) van der Werff (Lauraceae).[28] In the search for natural products of interest, *S. rubra* is a relevant model, of which the heartwood contains two major bioactive secondary metabolites rubrenolide (**1**) and rubrynolide (**2**) (Figure 1).[29] Rubrynolide shows a particularly potent termiticidal activity[30] while both rubrenolide and rubrynolide exhibit activity against pathogenic and lignivorous fungi[31,32] and mosquito larvae.[33] The bioassays suggest that these two compounds play a key role in heartwood resistance against wood destroying organisms.[34] Therefore, the *in situ* tandem mass spectrometry analysis can help to better understand the production of these metabolites within plant tissues, which might further contribute to the elucidation of their biosynthetic pathways.

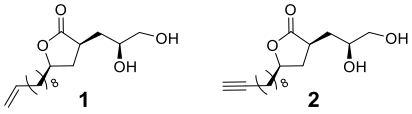

Figure 1: Structures of rubrenolide **1** and rubrynolide **2**.

MATERIALS AND METHODS

Plant material. Samples were collected from an *S. rubra* adult tree in the Paracou forest in French Guiana (5°15' N, 52°55'W) in December 2015. Wood increment cores were taken at a height of about 1 ~ 1.5 m, and stored frozen (-18 °C) until experiments were conducted. Each increment core contains both sapwood and heartwood which were separated when performing the ultramicrotomy.

Isolation of rubrenolide and rubrynolide. For extraction and isolation of chemical species, the wood sample was collected from commercial forest waste and identified by professional forest prospectors. Wood materials were ground into small particles of 0.5 mm in a Retsch ZM 200 mill (Eragny-sur-Oise, France). Extraction of the chemical species from the *S. rubra* heartwood was performed as follows. Briefly, 200 g of wood was extracted three times at room temperature for 48 h with ethyl acetate (3 × 500 mL). The ethyl acetate extract was then purified by preparative chromatography on a Discovery C18 column (15 cm × 4.6 mm, 5 µm, Supelco) using a Waters HPLC system equipped with a W2996 photodiode array absorbance detector and a W2424 light-scattering detector. Water (HPLC grade) was obtained from a Milli-Q system (Milli-Q plus, Millipore Bedford, MA). Isolation of heartwood compounds rubrynolide and rubrenolide was carried out with 40 mg of the purified fraction diluted in 1.5 mL of water/acetonitrile 50:50 using a linear gradient of water/acetonitrile (50:50 to 0:100 over 15 min) and remaining at 100% acetonitrile during 5 min. The eluates from the column were monitored at 210 and 240 nm wavelengths, and the chromatographic profiles were consistent with ELSD detection in analytical mode using the same elution method at 1 mL/min. Fractions containing the same constituents were gathered and evaporation allowed for isolation of compounds rubrynolide (14.1 mg, 35.2% w/w) and rubrenolide (8.1 mg, 20.2% w/w). Both compounds were isolated in pure form.

LC-MS analysis. Purified rubrenolide and rubrynolide were prepared in methanol at a concentration of 0.1 mg/mL. LC-MS/MS experiments were performed on a HPLC Ultimate 3000 system (Dionex, Voisins-le-Bretonneux, France) coupled with an Agilent 6540 Q-ToF (Agilent Technologies, Waldbronn, Germany) mass spectrometer equipped with electrospray ion source. LC analysis was carried out in an Accucore RP-MS column (100 × 2.1 mm, 2.6 µm, Thermo Scientific, Les Ulis, France) with a mobile phase consisting of water (A) and acetonitrile (B). 0.1% formic acid was added to both phases. Compounds were eluted at a flow rate of 0.4 mL/min with a gradient from 5% B to 100% B in 25 min and then 100% B for 3 min. All the mass spectra were recorded in positive ion mode with the following parameters: spray voltage set at 3.5 kV, capillary temperature at 325 °C, capillary voltage at 45 V and 'fragmentor voltage' at 120 V. The collision energy was fixed at 15 eV for MS/MS fragmentation, which could provide rich fragment ions while still being able to preserve a certain amount of precursor ions in the spectra. Internal calibration was achieved with two known ion masses (m/z 121.0509 and m/z 922.0098) providing a high mass accuracy better than 2 ppm. Mass resolution (FWHM, full width at half maximum) was chosen at 20,000 for m/z 922 in MS and MS/MS spectra.

Wood surface preparation. The transition zone area of a wood increment core was first cut off by an electric saw. The small wood block (~ 0.7 cm × 0.7 cm × 0.7 cm) was then trimmed with a razor blade to generate a transverse cutting surface of approximately 1 mm × 2.5 mm which was left to be cut with ultramicrotome (EM UC6, Leica Microsystèmes, SAS, Nanterre, France) using a diamond knife (DIATOME Cryotrim 45°, Leica Microsystèmes, SAS, Nanterre, France). A high cutting speed of 50 mm/s was used considering the hard transverse wood surface and the cutting feed was set at 200 nm. The clearance angle was kept constant at 6° during the sectioning. An optical image of the wood surface was acquired at 10× magnification with an Olympus BX51 microscope (Rungis, France) and a Color View I camera, monitored by Cell^B software (Soft Imaging System, GmbH, Münster, Germany), using extended focal imaging (EFI) scanning mode.

TOF-SIMS tandem MS analysis. The parallel imaging MS/MS analyses were performed with the newly designed

TRIFT spectrometer on a PHI *nano*TOF II TOF-SIMS instrument (Physical Electronics, Minnesota, USA). A detailed description of the instrumental design has been presented by Fisher and colleagues.[25,26] Briefly, after desorption, the secondary ions are extracted into a TRIFT spectrometer which consists of three electrostatic analyzers (ESA). After the third ESA, an electrodynamic precursor selector is positioned so that the mass resolved ions can either fly through this crossover and be detected by the standard TOF-SIMS detector (MS1 in Figure 2) or be deflected into a collision cell for fragmentation (Figure 2). The fragment ions as well as the remaining precursor ions are then bunched and accelerated into a linear TOF analyzer before reaching the MS/MS detector (MS2 in Figure 2). The precursor selection window is monoisotopic (1 amu). Each pulse of the primary ion beam simultaneously triggers the time-of-flight clock in both spectrometers; hence, an exogenous calibration standard is not needed. In each acquisition, the deflected proportion of the precursor ions can be defined as desired so that it is possible to maintain a fractional portion of the precursor ions in the precursor ion spectrum.

In the current report, all the spectra and images were recorded with 30 keV Bi_3^+ primary ion beam of which the DC current was ~ 11 nA in all cases. The ion beam was operated in either the bunched mode or the un-bunched mode, with the former for high mass resolution spectra acquisition and the latter for best lateral resolution imaging. During the analysis, low energy electrons (15 eV) and low energy Ar^+ ions (10 eV) were applied for charge compensation. The field-of-view of each analytical area was 150 µm × 150 µm or 200 µm × 200 µm which was divided by 256 × 256 image pixels. Analysis was also conducted on a 300 µm × 300 µm area divided by 512 × 512 image pixels. In MS/MS acquisitions, the deflection fraction of the precursors into collision cell was 100% given the low abundance of target metabolites in the wood samples. In the precursor selector, precursor ions were deflected at ~1.5 keV, implying a keV collision event with the argon gas in the collision cell. The MS/MS acquisition time for each molecule was about 22 min at 256 × 256 pixels or 44 min at 512 × 512 pixels, and the respective primary ion beam density was 2.07×10^{13} or 1.26×10^{13} ions/cm² where stable ion emissions were recorded in the profiles. The lateral resolution ($\Delta\ell$) was measured in the 512 × 512 pixel analyses to be ≈ 400 nm. Mass spectra were acquired over a mass range of 0-1,000 in positive ion mode. In addition to the use of common fragments ($C_2H_5^+$, *m/z* 29.04; $C_3H_7^+$, *m/z* 43.05; $C_4H_9^+$, *m/z* 57.07) for mass scale calibration, improved mass accuracy at high *m/z* was achieved with internal fragments from wood structural polymer ($C_7H_7^+$, *m/z* 91.05; $C_7H_9^+$, *m/z* 93.07; $C_7H_{11}^+$, *m/z* 95.09; $C_8H_9^+$, *m/z* 105.07, and $C_{11}H_9O_3^+$, *m/z* 189.06), according to Goacher *et al.*[35] and Vanbellingen *et al.*[36] Data processing was performed using PHI TOF-DR (Physical Electronics, Minnesota, USA) software.

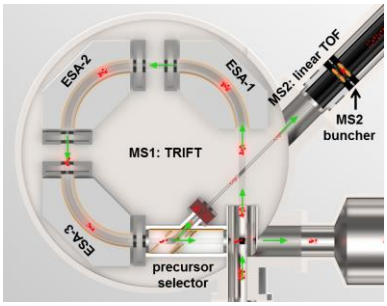

Figure 2: Schematic illustration of the parallel imaging MS/MS spectrometer. Adapted from 25.

RESULTS AND DISCUSSION

Structural characterization of isolated rubrynolide and rubrenolide by LC-MS/MS. The bioactive metabolites rubrynolide and rubrenolide, isolated from the wood extract, were first analyzed by LC-MS/MS. Figure 3 presents their LC profiles and the corresponding mass spectra. With the experimental conditions described above, the two metabolites were eluted at 11.46 min and 13.51 min, respectively. In the mass spectrum obtained from the peak at 11.46 min, *m/z* 297.2060, *m/z* 319.1879 and *m/z* 615.3881 were attributed to protonated rubrynolide ($C_{17}H_{29}O_4^+$, $\Delta_{m/z}$ = – 0.47 ppm) and its sodiated monomer ($C_{17}H_{28}O_4Na^+$, $\Delta_{m/z}$ = – 0.14 ppm) and dimer $C_{34}H_{56}O_8Na^+$, $\Delta_{m/z}$ = 2.27 ppm), respectively. Similarly, the peaks corresponding to $[M+H]^+$ (*m/z* 299.2213, $\Delta_{m/z}$ = – 1.30 ppm), $[M+Na]^+$ (*m/z* 321.2038, $\Delta_{m/z}$ = 0.53 ppm), and the $[2M+Na]^+$ (*m/z* 619.4188, $\Delta_{m/z}$ = 1.23 ppm) ions of rubrenolide ($C_{17}H_{30}O_4$, MW 298.213 g/mol) were also assigned (Figure 3d). To provide further structural characterization and to facilitate the comparison with the *in situ* TOF-SIMS MS/MS spectra, Q-TOF MS/MS fragmentation of the molecular precursor ions was carried out. The MS/MS spectra of the ions at *m/z* 297.2065 ($[M+H]^+$, rubrynolide) and *m/z* 299.2224 ($[M+H]^+$, rubrenolide) are shown in Figures 3e and 3f, respectively. According to the chemical structures of rubrenolide (**1**) and rubrynolide (**2**), the losses of water molecules in the high mass range occur from the hydroxyl groups and the γ-lactone ring opening.[37] The presence of hydrocarbon fragments with 12 amu or 14 amu mass intervals in the low mass range correspond to the fragmentation of the long carbon chain. All the peak attributions of the fragment ions shown in the spectrum are made within 5 ppm mass accuracy.

***In situ* detection and localization.** *In situ* mass spectrometric detection was performed on the transition zone of *S. rubra* wood sample with the knowledge that this area, located between sapwood and heartwood, is associated with the biosynthesis of wood metabolites during heartwood formation.[38] This localized biochemical process is supported by the significantly higher concentrations of metabolites in the transition zone due to the activation of metabolic pathways, as previously reported.[39] Figure 4 shows the mass spectrum recorded from a 150 µm × 150 µm area, of which the optical image is shown in Figure 5a. The primary ion beam was bunched to get a high mass resolution spectrum. Despite the possible topography of the wood tissues, a high mass resolution of 10,000 at *m/z* 263 was readily attained. This clearly indicates that very little topographic effect can be attributed to this sample, otherwise the mass resolution would be dramatically degraded. As illustrated in the inset of Figure 4, the protonated rubrynolide and rubrenolide were detected at very low intensity which is likely due both to the low ionization efficiency and to the low abundance of these metabolites in the wood tissue. Nevertheless, after internal mass calibration, as described above, a good mass accuracy below 10 ppm was achieved. The corresponding ion images of these two metabolites are shown in Figure 5 which reveals that rubrynolide and rubrenolide are colocalized around mainly ray parenchyma cells and small vessels (white arrows in Figures 5c and 5d). Ray parenchyma cells are the only living cells at the heartwood periphery, and many optical[40,41] and mass spectrometric[39] observations suggest that heartwood metabolites are primarily produced inside

these cells of the transition zone. Therefore, our imaging results support the notion that rubrynolide and rubrenolide are most probably biosynthesized in ray parenchyma cells, before being actively or passively transferred to nearby cells and tissues. However, TOF-SIMS imaging alone cannot provide conclusive identification owing to the limited mass resolution and mass accuracy. Moreover, TOF-SIMS data are comprised of an elevated noise baseline in comparison to corresponding tandem MS data.[25,42,43] Tandem MS imaging is thus required for both more confident identification and accurate molecular imaging.

***In situ* MS/MS characterization of rubrynolide and rubrenolide.** To guarantee a sufficient amount of precursor ions for MS/MS fragmentation, the electrodynamic precursor selector was operated in continuous mode and the ions at *m/z* 297 and *m/z* 299 were thoroughly deflected into the collision cell. Here, TOF-SIMS imaging and MS/MS imaging data were collected simultaneously and we can clearly observe the missing precursor ions in the TOF-SIMS spectra (data provided in Figures S1 and S2). The resulting tandem MS spectra are shown in Figure 6, with characteristic fragments of rubrynolide and rubrenolide.

As expected, and revealed in Figure 6a, successive loss of the two hydroxyl groups from the rubrenolide molecule, *via* neutral losses of water (H_2O), was quite pronounced after collision-induced dissociation (CID), leading to the product ions at *m/z* 281 ($C_{17}H_{29}O_3^+$) and *m/z* 263 ($C_{17}H_{27}O_2^+$), respectively. We also observed, at much lower intensity, the product ions arising from fragmentation of the γ-lactone ring. Ostensibly, the ether oxygen is involved in a neutral loss of water resulting in the product ion at *m/z* 245. The carbonyl oxygen was observed in the MS/MS spectrum of the purified rubrenolide (see Figure S3a) to be lost *via* two fragmentation paths; either by neutral loss of water producing an ion at *m/z* 227 or by neutral loss of carbon monoxide (CO) producing an ion at *m/z* 217. Given the low abundance of the metabolite precursor ions in the wood samples, the *m/z* 227 and *m/z* 217 product ions are not readily observed in the MS/MS spectrum from the *in situ* measurement. Following the losses of oxygen from the hydroxyl moieties and from the γ-lactone ring, and a neutral loss of ethylene (C_2H_4), we observe the product ion at *m/z* 199 ($C_{15}H_{19}^+$). The product ion series beginning at *m/z* 199 and below displays mass intervals of 12 amu (C), 14 amu (CH_2), 26 amu (C_2H_2) and 28 amu (C_2H_4) which is a typical fragmentation pattern observed with compounds bearing long hydrocarbon chains. The losses described above, and the abundant fragments in the low mass range, are in good accordance with those from Q-TOF MS/MS measurements and are attributed accordingly.

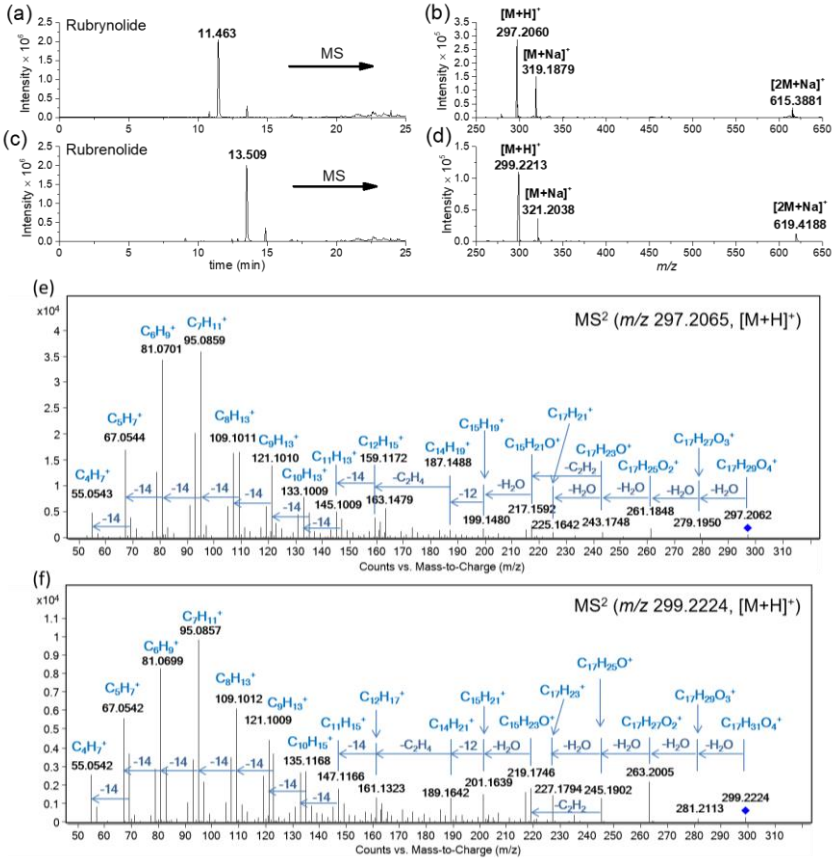

Figure 3: LC-MS analyses of the isolated bioactive compounds. (a) Liquid chromatogram of rubrynolide. (b) ESI-Q-TOF mass spectrum of rubrynolide. (c) Liquid chromatogram of rubrenolide. (d) ESI-Q-TOF mass spectrum of rubrenolide. (e) ESI-Q-TOF MS/MS spectrum of protonated rubrynolide (*m/z* 297.2065); (f) ESI-Q-TOF MS/MS spectrum of protonated rubrenolide (*m/z* 299.2224).

TOF-SIMS tandem MS imaging provides a self-consistent approach for molecular identification. We have stated earlier that no exogenous calibration reference is needed in MS/MS because each pulse of the primary ion beam simultaneously

triggers the time-of-flight clock in the TOF-SIMS and the MS/MS spectrometers (*i.e.* in the time-to-digital converter [TDC] electronics). Note, also, that the 52 μs duty cycle of MS/MS spectrometer is completed within the 120 μs duty cycle of the TOF-SIMS spectrometer. Hence, we begin with the mass scale intercept and the precursor mass-to-charge ratio based on the TOF-SIMS timings. The product ion mass scale calibration may be enhanced with the addition of putative peak compositions. Compositional assignments may be judged as correct or incorrect based on their effect on the mass scale calibration, *i.e.* the mass deviations (amu) and the mass accuracy ($\Delta_{m/z}$) as well as the correlation coefficient (R) of the overall calibration fit. Ideally, one would like R > 0.99 and $\Delta_{m/z}$ < 5 ppm. Subsequent to assignment of the putative structures for the product ions detailed above, the ascribed compositions were employed in the MS/MS calibration; the resulting mass accuracy was +3.69 ppm. High confidence was reached in the identification of the *m/z* 299 precursor as the $[M+H]^+$ ion of rubrenolide ($C_{17}H_{30}O_4$) within a mass error of 0.0011 amu.

Similarly for rubrynolide, revealed in Figure 6b, successive loss of the two hydroxyl groups from the precursor molecule *via* neutral losses of water (H_2O) was quite pronounced, leading to the product ions at *m/z* 279 ($C_{17}H_{27}O_3^+$) and *m/z* 261 ($C_{17}H_{25}O_2^+$), respectively. Product ions arising from fragmentation of the γ-lactone ring were also observed; the ether oxygen is cleaved through a neutral loss of water resulting in the product ion at *m/z* 243 while the carbonyl oxygen is thought to be expelled *via* either neutral loss of water producing an ion at *m/z* 225 or neutral loss of carbon monoxide producing an ion at *m/z* 215. Again, the *m/z* 225 and *m/z* 215 product ions are readily observed in the MS/MS spectrum of the purified rubrynolide (see Figure S3b) but are quite weak in the MS/MS spectrum from the *in situ* measurement. We observed the product ions at *m/z* 197 ($C_{15}H_{17}^+$) following the losses of oxygen from the hydroxyl moieties and from the γ-lactone ring. Finally, the product ion series beginning at *m/z* 197 and below display mass intervals of 12 amu (C), 14 amu (CH_2), 26 amu (C_2H_2) and 28 amu (C_2H_4) which is characteristic of the precursor molecule bearing a long hydrocarbon chain. The enumerated losses and the abundant fragments in the low mass range are in good accordance with those from Q-TOF MS/MS measurements. The ascribed compositions were utilized in the MS/MS calibration and the resulting mass accuracy was +4.52 ppm for identification of the *m/z* 297 precursor as the $[M+H]^+$ ion of rubrynolide ($C_{17}H_{28}O_4$), within a mass error of 0.0014 amu.

The keV fragmentation of rubrenolide and rubrynolide, *i.e.* the TOF-SIMS tandem MS measurements both *in situ* and of the purified compounds, results in very similar product ions to those produced by eV fragmentation, *i.e.* the Q-TOF measurement of the extracts. This is remarkable because the CID mechanisms at eV collision energy are different from those occurring at keV energies. The exotic peak at *m/z* 209 is neither observed in the low energy CID spectra of the extracts nor in the high energy CID spectra of the purified compounds. Since the *m/z* 209 product ion is not observed in the MS/MS spectra of the extracted or purified compounds, it is unlikely that it arises from a different fragmentation mechanism specifically associated with the high energy collisions. More simply, this product ion likely arises from an isobaric precursor ion, not separated from the rubrynolide in the 1 amu precursor selection window. However, this exotic peak does not downgrade the value or validity of the data, which shows that the principal precursor ions are those of rubrenolide and rubrynolide.

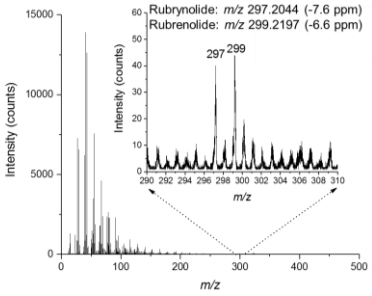

Figure 4: TOF-SIMS mass spectrum of an *S. rubra* wood sample from the transition zone (positive ion mode). The analysis area was 150 μm × 150 μm. The inset shows the spectrum of low abundance bioactive metabolites rubrynolide (*m/z* 297) and rubrenolide (*m/z* 299).

The MS/MS imaging data shown in Figure 7 were acquired on the same area as presented in Figure 5. These total ion current (TIC) images were obtained with all tandem MS product ions and unfragmented precursor ions from the selected precursor windows which were centered at *m/z* 297.20 (rubrynolide, Figure 7a) and *m/z* 299.21 (rubrenolide, Figure 7b). It is worth noticing that the monoisotopic selection of precursor ions effectively excludes the background interferences that are present in the TOF-SIMS data, leading to more reliable localization information of the target biomolecules. The described background, or "chemical noise", present in the TOF-SIMS data arises from a combination of in-source decay and post-source decay of molecules. The chemical background is almost entirely removed in MS/MS because there is a corresponding energy selection that takes place with the *m/z* selection; hence, the majority of ions originating from the chemical background never enter the collision cell, and those few ions that do enter the CID cell do not reach the MS/MS detector within the 52 μs duty cycle. The chemical background is not necessarily a high signal, but when imaging ions of low abundance the small background can easily obscure the molecular distribution(s) one desires to discern. The distributions of rubrynolide and rubrenolide, displayed in Figure 7a and 7b, are binned and scaled identically to those in Figures 5c and 5d. The MS/MS images (Figure 7) offer an accurate visualization of the bioactive metabolite distributions while the distributions furnished in the TOF-SIMS images (Figure 5) are skewed by background counts. As shown in the MS/MS ion images, rubrenolide and rubrynolide are colocalized principally in and around the ray parenchyma cells, which reinforces the hypothesis that the synthesis of these two bioactive metabolites in *S. rubra* wood occurs in ray parenchyma cells.

Figure 8 provides another example of TOF-SIMS tandem MS imaging from a different area of the transition zone. The lateral resolution was measured to be ≈ 400 nm as shown in Figures S6 through S9, which is easily achieved as reported in other studies,[42,43] and allows the observation of individual cell structures in the wood specimens. In this analysis area, we observed what appears to be a mis-cut oil cell located in proximity to both a vessel and ray parenchyma cells. In the immediate vicinity of this oil cell, we observed elevations of Na^+ and K^+ ion signals. In comparison to the *m/z* 297 and 299 ions of rubrynolide $[M+H]^+$ and rubrenolide $[M+H]^+$, we also observed an elevation in the TOF-SIMS signals arising at *m/z* 319, 321, 335, 337, 403, 405, 419 and 421. The ions at *m/z* 319, 321, 335, 337 we expected should be the $[M+Na]^+$ and $[M+K]^+$ ions of the

rubrynolide and rubrenolide metabolites because these ions were observed to be collocated with the Na^+ and K^+ ions. The other ions were previously not reported, and we thought there may be present some compounds which were involved in the metabolic pathway that produces rubrynolide and rubrenolide. Specifically, as shown in Figures 8a and 8b, there is a colocalization of $^{41}K^+$ (*m/z* 41) and an heretofore unknown molecule at *m/z* 421 which we have labeled as $[M^{P3}+K]^+$. The relative distribution of protonated molecular ions and alkali adducts of molecular ions are exemplified in Figures 8a, 8e and 8f, while Figures 8c and 8d reveal the distribution of the aromatic and lignin species in the area of the oil cell. Note that in Figure 8b we have presented an image of the minor isotope ion peak of potassium, $^{41}K^+$ (*m/z* 41), because the major isotope ion peak of potassium, $^{39}K^+$ (*m/z* 39), was saturated.

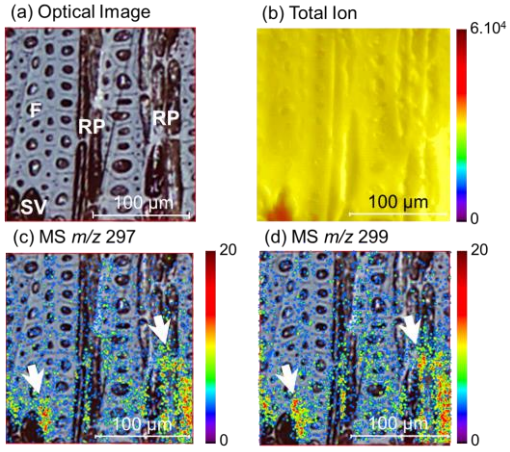

Figure 5: (a) Optical image of the analytical area on the transition zone wood sample. RP: ray parenchyma cell; F: fiber cell. SV: small vessel. (b) TOF-SIMS total ion image. (c) TOF-SIMS ion image of rubrynolide (*m/z* 297). (d) TOF-SIMS ion image of rubrenolide (*m/z* 299). The images (c) and (d) are overlaid on (a) the optical image. The analyzed area was 200 µm × 200 µm divided by 256 × 256 pixels. Ion images were compressed to 128 × 128 pixels to increase the contrast. White arrows indicate the apparent distribution of rubrynolide and rubrenolide near the small vessel and ray parenchyma cells.

TOF-SIMS tandem MS imaging was conducted with precursor selection of the *m/z* 421 ions; the resulting MS/MS spectrum is presented in Figure 8j, and the MS/MS images are shown in Figures 8a and 8g-8i. Note that the $[M^{P3}+K]^+$ images given in Figures 8a and 8g are both of the MS/MS total ion counts (TIC), and the only differences are the field-of-view and the color scale. Without expansion of the intensity scale in the MS/MS spectrum, a solitary product ion attributed to K^+ was observed at *m/z* 39. This single piece of evidence was sufficient to support the notion that the *m/z* 421 precursor was a potassium adduct ion. However, we desired to determine the structure of this unidentified molecule.

The prominent peaks of the MS/MS product ion spectrum may be attributed with a rudimentary understanding of the keV collision induced dissociation. First, there are only rare cases when multiply charged secondary ions are observed in TOF-SIMS; therefore, the precursor ion is always assumed to have a single charge. Consequently, any product ion observed in an MS/MS spectrum must have arisen by a neutral loss from the precursor ion. An alkali element will almost never dissociate as a neutral atom; hence, the appearance of a very prominent K^+ peak in the MS/MS product ion spectrum. We must also consider potassium dissociation via some other channel, e.g. as part of a neutral molecular fragment. Moreover, the probability of multiple collisions or significant rearrangement products are negligible because the MS/MS duty cycle was only 52 µs and the transit time of precursor ions through the collision cell was less than one microsecond (< 1 µs). Given these boundary conditions, the identification of product ion peaks was relatively straight forward. Finally, putative peak attributions were made only where a single or dominant dissociation channel was apparent. For instances where multiple dissociation channels were evident we, in some cases, made a tentative peak attribution.

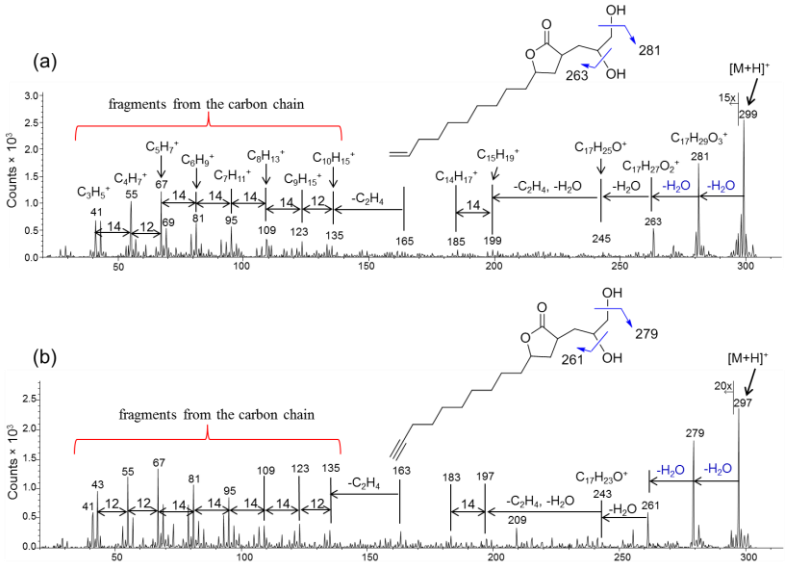

Figure 6: TOF-SIMS MS/MS spectra of (a) *m/z* 299 ($[M+H]^+$, rubrenolide) and (b) *m/z* 297 ($[M+H]^+$, rubrynolide). The blue-colored arrows in the structures indicate the characteristic loss of hydroxyl groups.

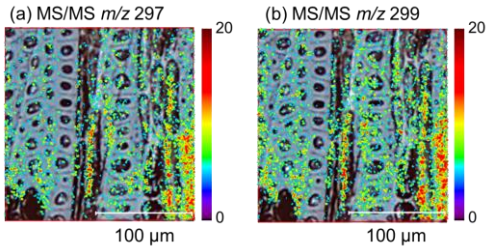

Figure 7: Tandem MS ion images of (a) rubrynolide (*m/z* 297) and (b) rubrenolide (*m/z* 299). The analytical area is the same as that in Figure 5, and the ion images are overlaid on the optical image of Figure 5a. The ion images were compressed from 256 × 256 pixels to 128 × 128 pixels to increase the contrast. The tandem MS images more accurately reveal the distributions of rubrynolide and rubrenolide which is observed primarily in and around the RP cells. The chemical background that is prevalent in the TOF-SIMS images is not present in the MS/MS images.

From the *m/z* 421 precursor we observed neutral losses of H_2O (18 amu) and CO (28 amu), resulting in product ions at *m/z* 403 and 393, respectively. A neutral loss of acetic acid (60 amu) from the precursor was observed to produce the $C_{19}H_{30}O_4K^+$ product ion at *m/z* 361; a further neutral loss of oxiran-2-one (58 amu) was observed to produce the $C_{17}H_{28}O_2K^+$ product ion at *m/z* 303. In coexisting dissociation channels, a neutral loss of either potassium acetate or C_7H_{14} (98 amu) from the *m/z* 421 precursor may produce either $C_{19}H_{31}O_4^+$ or $C_{14}H_{20}O_6K^+$ product ions at *m/z* 323.

From *m/z* 303, concomitant neutral losses of buta-1,2,3-triene (52 amu) and ethylene (28 amu) were observed, ending with the $C_{14}H_{25}O_2^+$ product ion at *m/z* 225. We also observed the potential losses of acetic acid (60 amu) and potassium acetate (98 amu) from the *m/z* 421 precursor resulting in the product ion at *m/z* 263. The m/z 263 attribution remained tentative, either $C_{17}H_{28}O_2^+$ or $C_{14}H_{24}O_2K^+$, because there was also a neutral loss of acetic acid (60 amu) observed, originating from the *m/z* 323 product ion, and a neutral loss of prop-1,2-diene (40 amu), originating from the *m/z* 303 ($C_{17}H_{28}O_2K^+$) product ion. Likewise, there are multiple dissociation channels observed which may have produced the *m/z* 225 product ions. There were two dissociation channels recognized initially to generate the product ions at *m/z* 165; a neutral loss of potassium acetate (98 amu) from the *m/z* 263 product ion peak, and a neutral loss of acetic acid (60 amu) from the *m/z* 225 product ion peak. However, there was observed another dissociation channel after to the combined losses of acetic acid and oxiran-2-one from the *m/z* 421 precursor. A neutral loss of $C_{10}H_{18}$ (138 amu) from the *m/z* 303 ($C_{17}H_{28}O_2K^+$) product ion peak, subsequent to the acetic acid and oxiran-2-one neutral losses, was observed to produce the *m/z* 165 product ion peak. The $C_{10}H_{18}$ neutral loss is likely and favorable because the bond cleavage occurs at the C-10 bond following the acetate cleavage having occurred at the C-11 bond (blue marker, inset Figure 8j). Successively, there was observed a neutral loss of prop-1,2-diene (40 amu) to produce the oxolan-2-one adduct ions at *m/z* 125 ($C_4H_6O_2K^+$).

The product ions at *m/z* < 125 display mass intervals of 12 amu (C), 14 amu (CH_2), 26 amu (C_2H_2) and 28 amu (C_2H_4) which is a typical fragmentation pattern observed with compounds bearing long hydrocarbon chains. In total, the MS/MS spectrum provided evidence of six oxygen atoms and at least two acetoxy group. The detection of the potassium ion adduct of oxolan-2-one in the *m/z* 421 $[M+K]^+$ product ion spectrum was a distinguishing breakthrough. Oxolan-2-one was not significant, either as an $[M]^+$ ion (*m/z* 86) or as an $[M+H]^+$ ion (*m/z* 87), in the $[M+H]^+$ product ion spectrum of either rubrynolide or rubrenolide (see Figure 6). Having recognized the foundational product ion as the potassium ion adduct of oxolan-2-one, it became apparent that every major product ion contained the potassium ion and that the neutral loss of potassium acetate was a minor or nonexistent dissociation channel. The putative identification of the oxolan-2-one adduct ion, together with evidence of two acetoxy group and an alkyl chain, is strong evidence that the precursor molecule is a γ-lactone. The neutral loss of $C_{10}H_{18}$ from the *m/z* 303 product ion peak is substantive evidence that the alkyl chain contains a double bond. Therefore, we posit that the molecule of the *m/z* 421 $[M+K]^+$ precursor is a γ-lactone having a hydrocarbon chain very similar in composition to that of rubrenolide and with two acetoxy groups.

Prior to the identification of the oxolan-2-one adduct ion (*m/z* 125), the ascribed putative compositions were applied in the MS/MS calibration; this calibration included product ions at *m/z* ≥ 125 having $C_XH_YO_Z^+$ and $C_XH_YO_ZK^+$ composition arising from neutral losses with and without the potassium atom, e.g. potassium acetate and acetic acid, respectively. Product ions at *m/z* < 125 were identified as $C_XH_Y^+$ ions of the alkyl chain. The resulting mass accuracy was observed to be +5.34 ppm. High confidence was reached, *i.e.* a calculated mass error of 0.0022 amu, in the designation of the *m/z* 421 precursor as the $[M+K]^+$ ion of the γ-lactone ($C_{21}H_{34}O_6$) shown in the inset of Figure 8j. However, following identification of the oxolan-2-one adduct ion, we concluded that every product ion at *m/z* ≥ 125 must be a potassium ion adduct. The putative compositions of prominent product ions are so identified in Figure 8j. The resulting mass accuracy was +0.20 ppm, *i.e.* a calculated mass error of 0.000084 amu, in identifying the *m/z* 421 precursor as the $[M+K]^+$ ion of the γ-lactone ($C_{21}H_{34}O_6$). Additional analyses to confirm this structural assignment are presently underway. Notwithstanding, all three γ-lactones are suspected to originate from the same metabolic pathway in *S. rubra*. As shown in Figures 8g-8i, the MS/MS total ion counts, the product ion sum and the K^+ product ions all map to the same location having high alkali ion signal (Figure 8b) within the oil cell as measured simultaneously by TOF-SIMS tandem MS imaging. These measurements seem to support the notion that (a) we have tentatively identified a γ-lactone compound by keV CID of the $[M+K]^+$ precursor and (b) the newly detected γ-lactone is likely related to the biosynthetic pathway of rubrynolide and rubrenolide.

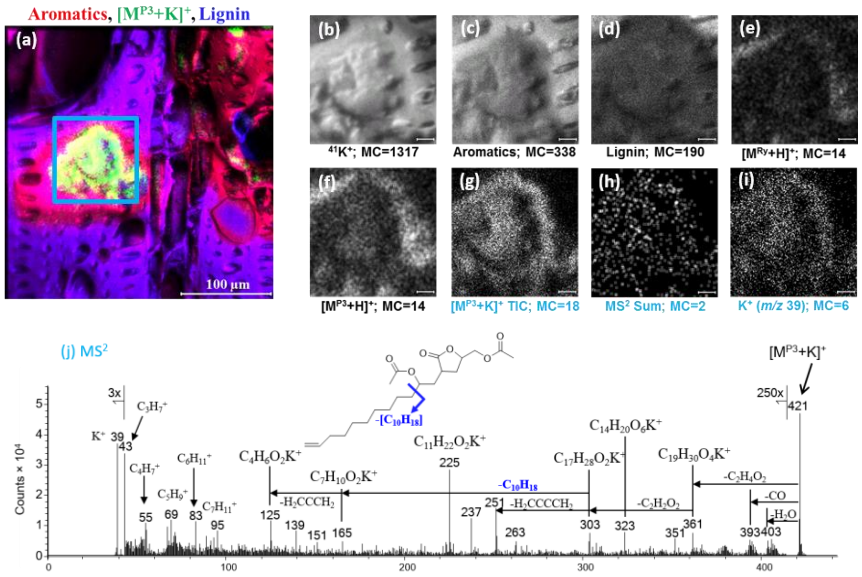

Figure 8: (a) A combined MS (MS^1) and MS/MS (MS^2) false color overlay of aromatic fragment ions (MS^1, *m/z* 77.04 and 91.06, red), the total ions of *m/z* 421 $[M^{P3}+K]^+$ (MS^2, green), and lignin fragment ions (MS^1, *m/z* 137.06, 151.08, 167.07 and 181.05, blue). The field-of-view is 300 µm × 300 µm acquired at 512 × 512 image pixels. The blue square indicates the 70 µm × 70 µm area expanded in the gray-scale images of panels (b) through (i). (b) MS^1 image of $^{41}K^+$ ions. (c) MS^1 image of the aromatic ion sum. (d) MS^1 image of the lignin ion sum. (e) MS^1 image of the rubrynolide metabolite $[M^{Ry}+H]^+$ ions, compressed to 128 × 128 pixels. (f) MS^1 image of the suspected biosynthetic $[M^{P3}+H]^+$ ions, compressed to 128 × 128 pixels. (g) Tandem MS (MS^2) image of *m/z* 421$[M^{P3}+K]^+$ ions (*i.e.* the sum of all product ions and unfragmented precursor ions). (h) MS^2 image of the product ions (*i.e.* *m/z* 303, 225, 125 and 43) arising from the $[M^{P3}+K]^+$ ions, compressed to 128 × 128 pixels. (i) MS^2 image of the K^+ product ions (*m/z* 39) arising from the $[M^{P3}+K]^+$ ions. (j) MS^2 spectrum arising from CID fragmentation of $[M^{P3}+K]^+$ (*m/z* 421) ions. The proposed γ-lactone molecular structure is shown in the inset.

CONCLUSION

The lack of a tandem mass spectrometry capability has long been an issue in applying TOF-SIMS imaging to biological studies, or any characterization requiring definitive structural characterization of molecules. Herein, TOF-SIMS tandem MS imaging was successfully applied to perform *in situ* characterization and localization of bioactive metabolites in tropical wood species *S. rubra*. The MS/MS imaging data significantly increased the confidence of the molecular identification and the localization of the bioactive metabolites rubrynolide and rubrenolide. MS/MS ion images exhibited superior image contrast which was useful to more precisely localize the low abundance biomolecules to anatomical structures; this is certainly needed for investigation of natural products as exemplified herein for a botanical subject. Both TOF-SIMS and MS/MS ion images demonstrate the colocalization of rubrenolide and rubrynolide principally in and around ray parenchyma cells, in agreement with previous work on the biosynthesis of wood metabolites. Notably, the distinctive tandem MS imaging analysis additionally reveals the contribution of oil cells for producing wood metabolites. In a future study, the biosynthetic pathway will be investigated with a thorough analysis of all the precursor ions which can be detected by *in situ* analysis, while also making use of complementary structural analysis methods like NMR and LC-MS/MS to obtain unambiguous identifications. Nevertheless, by TOF-SIMS tandem MS imaging alone, we have garnered unassailable evidence for a previously unreported γ-lactone molecule ($C_{21}H_{34}O_6$), co-localized with rubrenolide and rubrynolide, suggesting a common biosynthetic origin. These observations underpin the promise of TOF-SIMS tandem MS imaging for future studies in plant metabolism and biosynthesis.

ASSOCIATED CONTENT

Supporting Information. Figure S1: MS and MS/MS spectra, at 100% duty cycle, of the rubrynolide (*m/z* 297) precursor. Figure S2: MS and MS/MS spectra, at 100% duty cycle, of the rubrenolide (*m/z* 299) precursor. Figure S3: MS/MS spectra of the purified rubrenolide and rubrynolide references. Figures S4 and S5: original Figures 5 and 7. Figures S6 to S9: linescan measurements.

The Supporting Information is available free of charge on the ACS Publications website.

This work is part of the PhD thesis of TF: Tingting Fu. 3D and High Sensitivity Micrometric Mass Spectrometry Imaging. Analytical chemistry. Université Paris-Saclay, 2017. https://tel.archives-ouvertes.fr/tel-01699065v2/document (accessed 24 May 2018)

AUTHOR INFORMATION

Corresponding Authors

Gregory L. Fisher, E-mail: gfisher@phi.com
Alain Brunelle, E-mail: Alain.Brunelle@cnrs.fr

ORCID

David Touboul: 0000-0003-2751-774X
Gregory L. Fisher: 0000-0001-7517-0512
Alain Brunelle: 0000-0001-6526-6481
Christophe Duplais: 0000-0003-0926-9885

ACKNOWLEDGEMENTS

This work has benefited from an 'Investissement d'Avenir' grant managed by Agence Nationale de la Recherche (CEBA, ref. ANR-10-LABX-25-01) and the Agence Nationale de la Recherche (France, grant ANR-2015-CE29-0007-01 DEFIMAGE).

TF would like to acknowledge financial support from China Scholarship Council (CSC, No. 201406310013). The authors would like to thank Didier Stien for initiating this project.

REFERENCES

(1) Benguerba, M.; Brunelle, A.; Della-Negra, S.; Depauw, J.; Joret, H.; Le Beyec, Y.; Blain, M. G.; Schweikert, E. A.; Ben Assayag, G.; Sudraud, P. *Nucl. Instrum. Methods Phys. Res. B* **1991**, *62*, 8–22.
(2) Davies, N.; Weibel, D. E.; Blenkinsopp, P.; Lockyer, N.; Hill, R.; Vickerman, J. C. *Appl. Surf. Sci.* **2003**, *203-204*, 223–227.
(3) Kollmer, F. *Appl. Surf. Sci.* **2004**, *231-232*, 153–158.
(4) Touboul, D.; Kollmer, F.; Niehuis, E.; Brunelle, A.; Laprévote, O. *J. Am. Soc. Mass Spectrom.* **2005**, *16*, 1608–1618.
(5) Weibel, D.; Wong, S.; Lockyer, N.; Blenkinsopp, P.; Hill, R.; Vickerman, J. C. *Anal. Chem.* **2003**, *75*, 1754–1764.
(6) Tanaka, M.; Moritani, K.; Hirota, T.; Toyoda, N.; Yamada, I.; Inui, N.; Mochiji, K. *Rapid Commun. Mass Spectrom.* **2010**, *24*, 1405–1410.
(7) Winograd, N. *Anal. Chem.* **2005**, *77*, 142A–149A.
(8) Mochiji, K.; Hashinokuchiy, M.; Moritani, K.; Toyoda, N. *Rapid Commun. Mass Spectrom.* **2009**, *23*, 648–652.
(9) Brunelle, A.; Touboul, D.; Laprévote, O. *J. Mass Spectrom.* **2005**, *40*, 985–999.
(10) Bich, C.; Touboul, D.; Brunelle, A. *Mass Spectrom. Rev.* **2014**, *33*, 442–451.
(11) Fletcher, J. S.; Lockyer, N. P.; Vickerman, J. C. *Mass Spectrom. Rev.* **2011**, *30*, 142–174.
(12) McDonnell, L. A.; Heeren, R. M. A. *Mass Spectrom. Rev.* **2007**, *26*, 606–643.
(13) Touboul, D.; Brunelle, A. *Bioanalysis* **2016**, *8*, 367–369.
(14) Green, F. M.; Gilmore, I. S.; Seah, M. P. *J. Am. Soc. Mass Spectrom.* **2006**, *17*, 514–523.
(15) Touboul, D.; Brunelle, A.; Laprévote, O. *Rapid Commun. Mass Spectrom.* **2006**, *20*, 703–709.
(16) Carado, A.; Passarelli, M. K.; Kozole, J.; Wingate, J. E.; Winograd, N.; Loboda, A.V. *Anal. Chem.* **2008**, *80*, 7921–7929.
(17) Carado, A.; Kozole, J.; Passarelli, M.; Winograd, N.; Loboda, A.; Wingate, J. *Appl. Surf. Sci.* **2008**, *255*, 1610–1613.
(18) Lanni, E. J.; Dunham, S. J.; Nemes, P.; Rubakhin, S. S.; Sweedler, J. V. *J. Am. Soc. Mass Spectrom.* **2014**, *25*, 1897–1907.
(19) Fletcher, J. S.; Rabbani, S.; Henderson, A.; Blenkinsopp, P.; Thompson, S. P.; Lockyer, N. P.; Vickerman, J. C. *Anal. Chem.* **2008**, *80*, 9058–9064.
(20) Hill, R.; Blenkinsopp, P.; Thompson, S.; Vickerman, J. C.; Fletcher, J. S. *Surf. Interface Anal.* **2011**, *43*, 506–509.
(21) Rabbani, S.; Fletcher, J. S.; Lockyer, N. P.; Vickerman, J. C. *Surf. Interface Anal.* **2011**, *43*, 380–384.
(22) Phan, N. T. N.; Munem, M.; Ewing, A. G.; Fletcher, J. S. *Anal. Bioanal. Chem.* **2017**, *409*, 3923–3932.
(23) Smith, D. F.; Robinson, E. W.; Tolmachev, A. V.; Heeren, R. M.; Pasa-Tolic, L. *Anal. Chem.* **2011**, *83*, 9552–9556.
(24) Passarelli, M. K.; Pirkl, A.; Moellers, R.; Grinfeld, D.; Kollmer, F.; Havelund, R.; Marshall, P. S.; Arlinghaus, H.; Alexander, M. R.; West, A.; Horning, S.; Niehuis, E.; Makarov, A.; Dollery, C. T.; Gilmore, I. S. *Nat. Meth.* **2017**, *14*, 1175-1183.
(25) Fisher, G. L.; Bruinen, A. L.; Ogrinc Potočnik, N.; Hammond, J. S.; Bryan, S. R.; Larson, P. E.; Heeren, R. M. A. *Anal. Chem.* **2016**, *88*, 6433–6440.
(26) Fisher, G. L.; Hammond, J. S.; Larson, P. E.; Bryan, S. R.; Heeren, R. M. A. *J. Vac. Sci. Technol. B* **2016**, *34*, 03H126.
(27) Fletcher, J. S. *Analyst* **2009**, *134*, 2204–2215.
(28) van der Werff, H. *Novon* **1997**, *7*, 436–439.
(29) Madda, J.; Khandregula, S.; Bandari, S. K.; Kommu, N.; Yadav, J. S. *Tetrahedron Asymmetr.* **2014**, *25*, 1494–1500.
(3 0) Rodrigues, A. M. S.; Amusant, N.; Beauchêne, J.; Eparvier, V.; Leménager, N.; Baudassé, C., Espíndola, L. S.; Stien, D. *Pest Manag. Sci.* **2011**, *67*, 1420–1423.
(3 1) Houël, E.; Rodrigues, A.; Nicolini, E.; Ngwete, O.; Duplais, C.; Stien, D.; Amusant, N. IRG/WP 17-10887, **2017**, Proceedings IRG Annual Meeting (ISSN 2000-8953).
(3 2) Rodrigues, A. M. S.; Theodoro, P. N. E. T.; Eparvier, V.; Basset, C., Silva, M. R. R.; Beauchêne, J.; Espíndola, L. S.; Stien, D. *J. Nat. Prod.* **2010**, *73*, 1706–1707.
(3 3) Falkowski, M.; Jahn-Oyac, O.; Ferrero, E.; Issaly, J.; Eparvier, V.; Rodrigues, A. M. S.; Stien, D.; Houël, E.; Dusfour, I. *J. Am. Mosquito Contr.* **2016**, *32*, 337–340.
(3 4) Amusant, N.; Migg, M.; Thibaut, B.; Beauchene, J. *Int. Biodeter. Biodegr.* **2014**, *94*, 103–108.
(3 5) Goacher, R. E.; Jeremic, D.; Master, E. R. *Anal. Chem.* **2011**, *83*, 804–812.
(3 6) Vanbellingen, Q. P.; Fu, T.; Bich, C.; Amusant, N.; Stien, D.; Della-Negra, S.; Touboul, D.; Brunelle, A. *J. Mass Spectrom.* **2016**, *51*, 412–423.
(3 7) Crotti, A. E. M.; Bronze-Uhle, E. S.; Nascimento, P. G. B. D.; Donate, P. M.; Galembeck, S. E.; Vessecchia, R.; Lopes, N. P. *J. Mass Spectrom.* **2009**, *44*, 1733–1741.
(38) Beritognolo, I.; Magel, E.; Abdel-Latif, A.; Charpentier, J. P.; Jay-Allemand, C.; Breton, C. *Tree Physiol.* **2002**, *22*, 291–300.
(39) Saito, K.; Mitsutani, T.; Imai, T.; Matsushita, Y.; Fukushima, K. *Anal. Chem.* **2008**, *80*, 1552–1557.
(40) Hillis, W. E. *IAWA J.* **1996**, *17*, 405–419.
(41) Nagasaki, T.; Yasuda, S.; Imai, T. *Phytochemistry* **2002**, *60*, 461–466.
(42) Fisher, G. L., Hammond, J. S., Bryan, S. R., Larson, P. E., Heeren, R. M. A., *Microsc. Microanal.* **2017**, *23*, 843-848.
(43) Chini, C. E., Fisher, G. L., Johnson, B., Tamkun, M. M., Kraft, M. L., *Biointerphases* **2018**, *13*, 03B409(1-9).